

Adaptive response of a metal–organic framework through reversible disorder–disorder transitions

S. Ehrling,¹ E. M. Reynolds,² V. Bon,¹ I. Senkovska,¹ T. E. Gorelik,³ J. D. Evans,¹ M. Rauche,⁴ M. Mendt,⁵ Manfred S. Weiss,⁶ A. Pöpl,⁵ E. Brunner,⁴ U. Kaiser,³ A. L. Goodwin^{*,2} and S. Kaskel^{*,1}

¹Inorganic Chemistry Center I, Department of Chemistry, Technische Universität Dresden, Bergstr. 66, 01069, Dresden, Germany.

²Inorganic Chemistry Laboratory, Department of Chemistry, University of Oxford, South Parks Road, Oxford OX1 3QR, U.K.

³Electron Microscopy Group of Materials Science (EMMS), Central Facility for Electron Microscopy, Ulm University, Albert Einstein Allee 11, 89081 Ulm, Germany

⁴Chair of Bioanalytical Chemistry, Department of Chemistry, Technische Universität Dresden, Bergstr. 66, 01069, Dresden, Germany

⁵Felix Bloch Institute for Solid State Physics, Leipzig University, Linnéstr. 5, 04103, Leipzig, Germany

⁶Research Group Macromolecular Crystallography, Helmholtz-Zentrum Berlin für Materialien und Energie, Albert-Einstein-Straße 15, 12489 Berlin, Germany

*To whom correspondence should be addressed;

E-mail: andrew.goodwin@chem.ox.ac.uk or stefan.kaskel@tu-dresden.de.

Ultrahigh porosity and functionality bring porous metal-organic frameworks forward for applications ranging widely from gas storage and separation to catalysis and sensing. A unique feature of some frameworks is switchability, the ability to open their pores selectively in response to a specific guest enabling highly selective separation. A prerequisite for such a dynamic transformation is bistability of the host structure enabling the framework to breath, i.e. to switch between two stability minima in response to compositional changes in the fluid phase.

Here we describe a porous framework (DUT-8(Ni), DUT = Dresden University of Technology) adopting a configurationally-degenerate family of disordered states that respond adaptively to specific guest stimuli. This disorder originates from non-linear carboxylate linkers arranging paddle wheels in closed loops of different local symmetries that in turn propagate as tilings of characteristic complex superstructures. Solvent exchange stimulates the formation of distinct disordered superstructures for specific guest molecules as demonstrated by high resolution transmission electron microscopy and diffraction techniques. Remarkably, guest exchange stimulates repeatable switching transitions between distinct disorder states.

Introduction

Metal-Organic Frameworks (MOFs) have reached unexpected performance among other porous materials in terms of specific surface area, pore volume, functionality and structural variability^{1, 2, 3, 4, 5}. These developments have resulted in a wide range of applications which are either commercialized or under investigation for applications in gas storage, separation, catalysis, sensing, electronics and many more^{6, 7, 8}.

Flexibility is an important and appealing property exhibited by relatively few of the very many known MOFs^{9, 10}. In particular the ability to adapt the pore size to a guest molecule entering the pore system results in pronounced selectivity in gas separation^{11, 12, 13, 14}, an almost ideal deliverable storage capacity^{15, 16, 17} and novel enzyme-like responsivity of complex framework architectures¹⁸.

The very simplest prerequisite for flexibility is bistability, which allows switching between two distinguishable states in response to external stimuli. Canonical examples are the narrow and large pore states of breathing MOFs such as MIL-53¹⁹ or DUT-49^{20, 21}. More complex behaviour emerges for systems with more than one accessible state. For example, the essentially continuous pore opening of MIL-88²² and the induced-fit guest-recognition polymorphism of some hydrogen bonded frameworks¹⁸ collectively identify the importance of more complex configurational landscapes for optimising catalytic or sensing architectures.

The sophisticated dynamic energy-landscape of these switchable MOFs motivated us to explore in detail the behaviour of a prototypical switchable model system, namely DUT-8(Ni) ($[\text{Ni}_2(2,6\text{-ndc})_2\text{dabco}]_n$ (2,6-ndc = 2,6-naphthalenedicarboxylate, dabco = 1,4-diazabicyclo-(2,2,2)-octane). The basic structure of this MOF consists of paddle wheels (PW) connected by 2,6-ndc linkers to form two-dimensional square (4,4) grids; axial coordination by dabco results in a highly porous pillared layer structure (Figure 1a,b). Despite its similarity to long-known analogues containing simple terephthalate linkers (DMOF²³) and related systems, DUT-8(Ni) stands out demonstrating colossal stimuli-responsive switching transitions with up to 250% volume change induced by the adsorption of N₂ (77 K), CO₂ (195 K), Xe (165 K) alkanes and alkenes^{24, 25}. In-depth studies demonstrated not only the chemical composition^{26, 27} but also the particle size to massively affect the structural switching transition pressure^{28, 29}. DUT-8(Ni) is a highly selective adsorbent demonstrating

solvent recognition phenomena and a guest-dependant pore opening mechanism^{30, 31}.

However, in our attempts to optimize synthesis conditions and single crystal growth we observed an unexpected variation of X-ray diffraction patterns - both single-crystal and powder - that precluded unambiguous assignment of symmetry and structure solution (Figure 1c,d) and suggested a surprising degree of polymorphism in this material.

Previous computational studies proposed such polymorphism might arise from different linker orientations, with severe implications on the switching mechanism³². The authors applied well-tempered metadynamics calculations based on DFT-based Born–Oppenheimer potential energy surface as well as grand-canonical Monte-Carlo simulations and concluded restricted switchability depending on linker orientation. Here we demonstrate that DUT-8(Ni) is not polymorphic in the conventional sense, but rather adopts a degenerate family of disordered configurations. Remarkably, this configurational landscape can be navigated by guest sorption. This disorder-disorder switchability is fully reversible and multiple switching between distinct disorder variants is possible. X-ray and electron diffraction techniques in combination with high resolution transmission electron microscopy, solid state NMR and EPR studies provide insights into the microscopic switching mechanism.

Results

Discovery and rationalisation of disorder and structural diversity

In our initial attempts to understand the complex diffraction patterns observed experimentally, we carefully reconsidered all potential arrangements of the step-shaped linker and PW. The basic building block of the (4,4) net is a closed square loop, with PW complexes as nodes (vertices) connected by 2,6-ndc (edges) (Figure 1). The higher level of complexity arises from the non-linearity of the linker (Figure

1a), representing an individual “stair” with a step-height of 1.2 Å in a complex 3D “staircase” (i.e. the framework). PWs connected by 2,6-ndc are not in the same plane but arranged in alternating heights. On proceeding around any given loop, there must be as many “up” steps as “down” steps (i.e. two of each) in order to satisfy its natural boundary conditions. There are exactly six possible up/down arrangements, four of which result in a loop with C_{2h} point symmetry and the other two give D_{2d} symmetry (Figure 2a, Methods section, Extended Data Fig. 1, Extended Data Fig. 2).

Since neighbouring loops share edges, their corresponding states are not independent. The matching rules that emerge are captured by representing each loop by one of six “jigsaw” tiles (Figure 2a): any sensible jigsaw tiling corresponds to a physically sensible ensemble of 2,6-ndc orientations in the corresponding network structure.

A periodic concatenation of identically oriented (coloured) C_{2h} loops leads to an ordered tiling with monoclinic symmetry, earlier termed “polymorph B”³². Likewise, the (greyscale) D_{2d} loops can also give an ordered tiling with tetragonal symmetry (“polymorph A”, Extended Data Fig. 2)³². However, our conceptual analysis reveals these two polymorphs to represent only two limiting, ordered instances of a much larger configurational landscape (Figure 2b, Methods section, Extended Data Fig. 3, Extended Data Fig. 4). The statistical mechanics of the geometric model onto which our jigsaw tiling maps (the so-called “square-ice” model) is well understood, and the system is known to support a finite configurational entropy³³. In other words, the number of available DUT-8 configurations scales linearly with system size. This extensive configurational landscape contrasts the finite number of conformational states accessible even to protein-like hydrogen-bonded systems¹⁸, and also the continuous (but one-dimensional) spectrum of conformations in MIL-88 or SHF-61²²,³⁴. We identify specific DUT-8 states in terms of two parameters ϕ and η : the former

represents the likelihood of neighbouring rows/columns adopting opposite 2,6-ndc orientations and the latter is simply the relative fraction of D_{2d} loops. Geometry dictates that $\phi \geq \eta$, since D_{2d} loops can only tile by alternating 2,6-ndc orientations (Figure 2b, Extended Data Fig. 3).

Generating trial configurations and simulation of diffraction patterns

As the energetic landscape of correlated disordered states may severely impact the dynamic transformational behaviour and mechanical properties of the system it is essential to explain the unusual diffraction behaviour of DUT-8. We calculated PXRD patterns for a set of 55 structures in a 40×40 supercell of the parent DUT-8 framework structure covering a wide range of feasible configurations with varying ϕ, η values and compared them to our experimental powder diffraction data (Supplementary Section 4, Fig. 2-8). We find that the surprising diversity of PXRD patterns observed experimentally is reflected also by the powder diffraction patterns calculated from our simplistic ϕ, η landscape. Then, by matching the PXRD traces of various solvent filled DUT-8 variants to our calculations, we can estimate the ϕ, η values that best describe their corresponding structures (Figure 3a,b, Table 1, Extended Data Fig. 5). We note that the aim of this analysis is not to match quantitatively the observed peak intensities, since our structural models are intentionally simplistic (e.g. they do not contain guest molecules within pores). Instead our focus is on establishing the extent to which the configurational landscape shown in Figure 2b can explain simultaneously the variety of peak broadening and splitting observed in some regions of the diffraction pattern and also the preservation of sharp features in other regions of the diffraction pattern (Supplementary Fig. 3-8).

Not only do the as made frameworks (DMF) correspond to disordered configurations ($\phi = 0.4$, $\eta = 0.3$), but subsequent exchange with a wide range of solvents differing in size and polarity results in well-defined disordered configurations varying in ϕ and η (Figure 3b, Table 1). Amongst these, only the DCM-filled variant appears to contain a high fraction of D_{2d} loops (~70%) while all other solvents investigated contain only 0-30%. However, they differ markedly in ϕ (0.1-0.4) leading to pronounced differences in the experimental powder patterns (Figure 3a). The experimental evidence for these conclusions can be seen directly. For example, the reflections at $2\theta = 10\text{-}13^\circ$ appear particularly sensitive to 2,6-ndc orientations. Depending on these orientations, our PXRD patterns show either (i) a widening of the 111 peak, (ii) a splitting into 111 and $11\bar{1}$ or (iii) a narrowing of the 111 peak and an additional peak with low intensity at 10.5° (101). For example, *N*-methyl-2-pyrrolidone (NMP) and *n*-heptane induce the formation of a predominately monoclinic framework structure ($\phi = 0.1\text{-}0.3$, $\eta = 0.1\text{-}0.2$). Samples immersed in chloroform and tetrachloromethane contain mixtures of type 1 loops ($\phi = 0.4$, $\eta = 0.0$). Interestingly, only dichloromethane (DCM) induces linker orientations that correspond to an almost pure D_{2d} loop arrangement ($\phi = 0.9$, $\eta = 0.7$). These findings are also supported by single crystal analyses. In the case of as made crystals (containing DMF in the pores), tetragonal and monoclinic domains can be identified (Extended Data Fig. 6). However, single crystals with pores filled with NMP or toluene show preferably monoclinic domains in the reciprocal space (Supplementary Table 3, Extended Data Fig. 7) and resemble a four-component twin.

Electron diffraction and spectroscopic evidence of guest-controlled disorder

To clarify whether this characteristic disorder is truly persistent down to the nano-domain level and is not an artefact of our analysis we investigated DUT-8(Ni) nanocrystals via high resolution TEM and electron diffraction studies (Figure 4, Extended Data Fig. 8). Nanocrystals of DUT-8(Ni) are known to retain the open pore (*op*) structure upon desolvation^{28, 29}. The persistence of a metastable *op*-phase has been termed a “shape memory effect” and is akin to a martensitic transformation^{27, 35}. High resolution transmission electron microscopy (Figure 4b) and electron diffraction studies of as made (DMF) DUT-8(Ni) nanocrystals reveal whether distinct disorder patterns persist at nanodomain level (Figure 4c, Extended Data Fig. 8). Note that the simultaneous presence of both tetragonal (labelled ‘2’) and monoclinic (labelled ‘1, 3’) reflections in the single diffraction pattern of Figure 4c implies the coexistence of multiple domains within an as made single nanocrystallite. Inverse Fourier transformation (FT) analysis of the power spectra allows localisation of the corresponding domains in real-space. The presence of diffuse reflections is a clear indication for stacking faults in the structure. The deconvolution of diffuse reflections into several regions in $[1\bar{1}0]$ direction (as shown in projection in Figure 4d-f) demonstrates the simultaneous presence of nanodomains with tetragonal and monoclinic structure within one nanocrystal. This observation provides strong evidence that the interpretation of diffraction data based on the disorder model outlined above is reasonable (for more details see Methods section).

It should be emphasized that these disordered configurations imply the presence of four local PW configurations differing in local symmetry due to the relative arrangement of the surrounding “stairs” (Extended Data Fig. 3). These local configurations imply differences in continuous wave electron paramagnetic resonance (EPR) spectra through distinct variations of the local symmetry. Through deliberate doping, we introduce a spectator probe ion (Co^{2+}) into DUT-8(Ni) in low

concentration of DUT-8(Ni_{0.98}Co_{0.02}) (Supplementary Section 6). The incorporation of an EPR visible d⁷-probe in mixed-metal Ni²⁺-Co²⁺ PW units of the *op*-phase provides a *high spin* Co²⁺ ion ($S = 3/2$) coupling magnetically with a *high spin* Ni²⁺ ($S = 1$) to form a state with a total effective electron spin $S = 1/2$. Due to the hyperfine interaction (*hfi*) with the ⁵⁹Co nucleus ($I = 7/2$) evaluation of the sample specific g- and *hfi*-tensors gives insights into the local PW configuration. For the DCM loaded samples, the x and y principal values of the g- and *hfi*-tensors are close to each other, indicating a high degree of axial symmetry and suggesting that the corresponding PW units have an essentially fourfold rotational symmetry axis as expected for a high fraction of *D*_{2d} loops. However, for the as made (DMF) and *n*-heptane solvated samples the dominating 2,6-ndc coordination to the PW shows no fourfold symmetry axis. These spectroscopic signatures are in good agreement with the crystallographic analysis and disorder models developed.

Discussion

This guest-driven configuration control in distinctly disordered superstructures of a highly flexible MOF is an intricate phenomenon. Obviously, the host–guest interaction subtly directs the framework through energetic stabilization into a new disordered configuration – essentially an adaptive molecular response in the ϕ, η landscape – promoting a characteristic distribution of loops. Capturing specific solvent–host interactions represents a major challenge for simulation and modelling. However, it is chemically intuitive that differences in adsorption enthalpy and solvent packing will likely affect the structural equilibrium of the interacting host–guest system for different guests. In this context it is interesting to note the singular role of DCM which has a high adsorption enthalpy ($|\Delta_{\text{ads}}H| = 35 - 50 \text{ kJ mol}^{-1}$)²⁷ and dipole moment (1.8 D)³⁶. Molecular simulations indicate distinct solvent interactions for DUT-8(Ni) polymorphs

differing in symmetry uncovering a possible driving force for the disorder switching due to solvent-cluster interactions (Supplementary Section 10). DMF stimulates a preferred monoclinic conformation, whilst DCM shows a preferred tetragonal one. In addition, the relative energetic differences between these two extremes is higher for DCM compared to DMF. However, these initial estimations capture only a local picture and not the entire disordered configuration.

Recently switchability in frameworks has led to the discovery of unexpected **counterintuitive** phenomena such as negative gas adsorption (NGA)^{20, 21, 37, 38}. Switchability is a unique characteristic of a chosen few MOFs with the ability to adapt their pore size dynamically leading to extra-high selectivity in gas separation, ideal deliverable storage capacity in natural gas storage as well as promising sensing and catalytic functionality^{6, 7, 8, 11, 12, 13, 14, 15, 16, 17, 18, 39}. Hence, we were curious if switching between well-defined disordered configurations is achievable simply by repeated guest exchange.

By selecting two solvents resulting in markedly distinct powder patterns, namely DCM vs. DMF and DCM vs. *n*-heptane, we could indeed observe fully reversible switching between two disordered states (Figure 3c, Supplementary Fig. 12). The switching is easily discerned by following the evolution of the characteristic region of the X-ray diffraction pattern ($2\theta = 10\text{-}14^\circ$) demonstrating reversible switching between a configuration high in D_{2d} (DCM) and a predominately monoclinic one (DMF, *n*-heptane). In contrast, the macroscopic properties of the crystal such as morphology or particle size are not affected by the repeated solvent exchange (Supplementary Section 9, Fig. 15). Time-resolved studies indicate a complete conversion from one state into the other over ~30 minutes. Hence the configurational landscape of Figure 2b is at least partially navigable by suitable guest exchange chemistry. Even using

solvent mixtures (Figure 3d), the degree of disorder can be fine-tuned by gradually varying solvent ratio for example in the case of DCM in *n*-heptane.

The initial “as made” DUT-8 (DMF) assumes a configuration ($\phi = 0.4$, $\eta = 0.3$) differing from the one obtained after repeated exchange with DMF ($\phi = 0.3$, $\eta = 0.1$, Figure 3c, Table 1) and the initial “as made” disorder configuration cannot be restored, even by exchanging the solvent in the pores with a DMF/MeOH mixture, the same composition as applied in the synthesis (~2:1 v/v) (Supplementary Fig. 13). This underlines the importance of switching history on the structure of metal-organic frameworks in general, which is often overlooked⁴⁰.

Disorder-disorder switching may result either from (i) concerted rotation of 2,6-ndc linkers converting steps from up to down, associated with correlated translations of PW–dabco columns and microdomain boundaries moving through the crystal, or (ii) a dissolution–nucleation mechanism. The latter would imply that non-solvents for framework components, such as *n*-heptane, would suppress such a reversible transformation. This is clearly not the case. Hence navigation of the DUT-8(Ni) configurational landscape proceeds – remarkably – via concerted vertical translations of linear columns of alternating PW and dabco units shifting up and down, “*en bloc*”, throughout entire crystallites.

For an understanding of this movement it is important to clarify whether the 2,6-ndc linkers are permanently rotating in the solvated state, thermally activated pushing the PW columns up and down, or the transformation is a single event induced by a specific solvent–framework interaction. To answer this question, we recorded solid state NMR spectra of DUT-8(Ni) containing deuterated 2,6-ndc linkers in order to analyse the rotational mobility of the 2,6-ndc linker in equilibrium after solvent exchange (Figure 5). ²H NMR spectroscopy is a powerful tool for studying dynamic properties of solids.^{41, 42, 43, 44} The electric quadrupole interactions of the spins ($I = 1$)

dominate the spectra. Typically, the electric field gradient tensor for deuterons in C-D bonds is nearly axially symmetric⁴¹, which is advantageous to observe molecular motions as well as the orientational distribution in the presence of partial ordering⁴⁴. Various types of fast motion can be distinguished by evaluating characteristic line shapes of the ^2H spectra. Static deuteron NMR spectra of solids are very broad and typically cover a frequency range up to 250 kHz⁴³. To excite such a large frequency range and enhance the signal to noise ratio wide-line techniques like the WURST (wideband uniform-rate smooth truncation) pulse sequence combined with CPMG (Carr-Purcell Meiboom-Gill) pulse sequence were used⁴⁵. In the given case of Pake doublets (Figure 5), the distance between both intensity maxima (further denoted as peak separation) depends on fast motions of the linker molecules⁴⁶.

In Figure 5a, the peak separation is about 125 kHz, a typical value for immobile C-D groups, irrespective of the guests (Extended Data Fig. 1). Hence, the 2,6-ndc linkers do not perform thermally activated fast 180° flips irrespective of the solvent. Only DUT-8(Ni) as made (loaded with DMF) shows an additional signal in the middle of the spectrum with ca. 16 kHz line width. This small line width indicates a fast motion of a small fraction of the linkers, possibly indicating rotation of free linker coordinating with only one carboxylate group to the surface.

To also enable the detection of possible slow motions, we performed 2D EXSY (exchange spectroscopy) experiments on deuterated DUT-8(Ni). Comparison of calculated line shapes (Figure 5b) for various motions with experimental data in Figure 5c indicates that the linker is immobile up to the time scale of hundreds of milliseconds corresponding to rates of several Hertz. Over the temperature range of 243-343 K, there is no change in the ^2H NMR spectra visible. This indicates that temperature increase has no noticeable influence on linker mobility.

Consequently, our ^2H NMR measurements indicate that the majority (99%) of the linkers are interlocked after solvation and only a low concentration of freely-rotating linkers is detected with little variation for varying solvents. From this observation, a free thermally-activated rotation of the linker in the solvated framework at room temperature can be ruled out. Instead, each solvent locks the framework in a specific disordered superstructure configuration in the ϕ, η landscape. It is only by introducing a new guest that one stimulates the concerted reorientation of the framework constituents at once.

The disordered nature of DUT-8(Ni) has also profound implications for its dynamic pore closing mechanism. By analysing the pore closing dynamics of three prototypical cases representing a predominately tetragonal (DCM) vs. a monoclinic (*n*-heptane) domain architecture, and an intermediate case (as made - DMF) we find monoclinic domains to directly close their pores while tetragonal domains containing D_{2d} loops to rotate and adapt the linker orientations leading to C_{2h} loops (monoclinic domains) before pore closing into the closed pore (*cp*)-phase of DUT-8(Ni) (Supplementary Section 5, Fig. 9). This observation implies significant differences in the transformation mechanisms and trajectories of dynamic networks depending on their disorder configuration and may offer a strategy to tune the activation barriers and associated kinetics of adaptive pore structure transformations in future.

Summarizing, we have uncovered an **intricate** responsive behaviour in open frameworks involving interconversion between meaningfully-different disordered states. It is the specific type of symmetry lowering associated with stair-shaped framework components such as 2,6-ndc, that when combined with the underlying square lattice of the DUT-8(Ni) structure leads to an extensive configurational landscape. Host–guest interactions perturb the energetics of this landscape that the system responds adaptively to guest adsorption. Repeated solvent exchange

demonstrates reversible switching between distinct disordered states. This adaptive framework disorder-disorder switchability demonstrates a quasi-continuous dynamic transformation from one state into another. Each guest species encodes a complex microdomain structure (tiling) in the framework crystal recording the exposure history and molecular information in the material. The complex disorder pattern stores this type of information through the crystalline framework architecture⁴⁷. Given the multitude of non-linear linkers employed for the design of MOFs, COFs and more recently 2D materials we conceive disorder-disorder switchability to be of wider importance for framework materials than hitherto expected. Moreover, the control of disordered configurations may pave a way to encode open frameworks with complex information and consequently distinct implications for their physical characteristics such as optical, magnetic and micromechanics⁴⁷. In particular the activation energy and transformation rate of adaptive pore closing and opening phenomena are expected to become history dependent with important implications for the application of switchable MOFs in gas separation, storage and sensing devices⁴⁰.

References

1. Hönicke, I. M. *et al.* Balancing mechanical stability and ultrahigh porosity in crystalline framework materials. *Angew. Chem. Int. Ed.* **57**, 13780-13783 (2018).
2. Maurin, G., Serre, C., Cooper, A. & Ferey, G. The new age of MOFs and of their porous-related solids. *Chem. Soc. Rev.* **46**, 3104-3107 (2017).
3. Huang, Y.-B., Liang, J., Wang, X.-S. & Cao, R. Multifunctional metal–organic framework catalysts: synergistic catalysis and tandem reactions. *Chem. Soc. Rev.* **46**, 126-157 (2017).
4. Zhou, H.-C., Long, J. R. & Yaghi, O. M. Introduction to metal–organic frameworks. *Chem. Rev.* **112**, 673-674 (2012).
5. Stock, N. & Biswas, S. Synthesis of metal-organic frameworks (MOFs): routes to various MOF topologies, morphologies, and composites. *Chem. Rev.* **112**, 933-969 (2011).
6. Caro, J. Quo vadis, MOF? *Chem. Ing. Tech.* **90**, 1759-1768 (2018).
7. Fathieh, F. *et al.* Practical water production from desert air. *Sci. Adv.* **4**, eaat3198 (2018).
8. Chen, Y. *et al.* Stabilization of formate dehydrogenase in a metal–organic framework for bioelectrocatalytic reduction of CO₂. *Angew. Chem. Int. Ed.* 7764-7768 (2019).
9. Schneemann, A. *et al.* Flexible metal–organic frameworks. *Chem. Soc. Rev.* **43**, 6062-6096 (2014).
10. Lee, J. H., Jeoung, S., Chung, Y. G. & Moon, H. R. Elucidation of flexible metal-organic frameworks: research progresses and recent developments. *Coord. Chem. Rev.* **389**, 161-188 (2019).
11. Yang, S. *et al.* A partially interpenetrated metal–organic framework for selective hysteretic sorption of carbon dioxide. *Nat. Mater.* **11**, 710-716 (2012).
12. Duan, J. *et al.* High CO₂/N₂/O₂/CO separation in a chemically robust porous coordination polymer with low binding energy. *Chem. Sci.* **5**, 660-666 (2014).

13. Li, L. *et al.* Efficient separation of ethylene from acetylene/ethylene mixtures by a flexible-robust metal–organic framework. *J. Mater. Chem. A*. **5**, 18984-18988 (2017).
14. Taylor, M. K. *et al.* Near-Perfect CO₂/CH₄ selectivity achieved through reversible guest templating in the flexible metal–organic framework Co(bdp). *J. Am. Chem. Soc.* **140**, 10324-10331 (2018).
15. Mason, J. A. *et al.* Methane storage in flexible metal–organic frameworks with intrinsic thermal management. *Nature*. **527**, 357-361 (2015).
16. Li, H. *et al.* Recent advances in gas storage and separation using metal–organic frameworks. *Mater. Today*. **21**, 108-121 (2018).
17. Kundu, T., Wahiduzzaman, M., Bhuvan, B. S., Maurin, G. & Zhao, D. Solvent - induced control over breathing behavior in flexible metal-organic frameworks for natural - gas delivery. *Angew. Chem. Int. Ed.* **58**, 8073-8077 (2019).
18. Katsoulidis, A. P. *et al.* Chemical control of structure and guest uptake by a conformationally mobile porous material. *Nature*. **565**, 213-217 (2019).
19. Serre, C. *et al.* Very large breathing effect in the first nanoporous chromium(III)-based solids: MIL-53 or Cr^{III}(OH){O₂C–C₆H₄–CO₂}{HO₂C–C₆H₄–CO₂H}_xH₂O_y. *J. Am. Chem. Soc.* **124**, 13519-13526 (2002).
20. Krause, S. *et al.* A pressure-amplifying framework material with negative gas adsorption transitions. *Nature*. **532**, 348-352 (2016).
21. Krause, S. *et al.* Towards general network architecture design criteria for negative gas adsorption transitions in ultraporous frameworks. *Nat. Commun.* **10**, 3632 (2019).
22. Serre, C. *et al.* Role of solvent-host interactions that lead to very large swelling of hybrid frameworks. *Science*. **315**, 1828-1831 (2007).
23. Dybtsev, D. N., Chun, H. & Kim, K. Rigid and flexible: a highly porous metal–organic framework with unusual guest - dependent dynamic behavior. *Angew. Chem. Int. Ed.* **43**, 5033-5036 (2004).

24. Bon, V. *et al.* Exceptional adsorption-induced cluster and network deformation in the flexible metal–organic framework DUT-8(Ni) observed by in situ X-ray diffraction and EXAFS. *Phys. Chem. Chem. Phys.* **17**, 17471-17479 (2015).
25. Klein, N. *et al.* Monitoring adsorption-induced switching by ^{129}Xe NMR spectroscopy in a new metal–organic framework $\text{Ni}_2(2,6\text{-ndc})_2(\text{dabco})$. *Phys. Chem. Chem. Phys.* **12**, 11778-11784 (2010).
26. Klein, N. *et al.* Structural flexibility and intrinsic dynamics in the $\text{M}_2(2,6\text{-ndc})_2(\text{dabco})$ (M= Ni, Cu, Co, Zn) metal–organic frameworks. *J. Mater. Chem.* **22**, 10303-10312 (2012).
27. Ehrling, S. *et al.* Crystal size versus paddle wheel deformability: selective gated adsorption transitions of the switchable metal-organic frameworks DUT-8(Co) and DUT-8(Ni). *J. Mater. Chem. A*, **7**, 21459-21475 (2019).
28. Kavooosi, N. *et al.* Tailoring adsorption induced phase transitions in the pillared-layer type metal–organic framework DUT-8(Ni). *Dalton Trans.* **46**, 4685-4695 (2017).
29. Miura, H. *et al.* Tuning the gate-opening pressure and particle size distribution of the switchable metal–organic framework DUT-8(Ni) by controlled nucleation in a micromixer. *Dalton Trans.* **46**, 14002-14011 (2017).
30. Kavooosi, N. *et al.* Selective pore opening and gating of the pillared layer metal-organic framework DUT-8(Ni) upon liquid phase multi-component adsorption. *Microporous Mesoporous Mater.* **271**, 169-174 (2018).
31. Rauche, M. *et al.* New insights into solvent-induced structural changes of ^{13}C labelled metal-organic frameworks by solid state NMR. *Chem. Commun.* **55**, 9140-9143 (2019).
32. Petkov, P. S. *et al.* Conformational isomerism controls collective flexibility in metal–organic framework DUT-8(Ni). *Phys. Chem. Chem. Phys.* **21**, 674-680 (2019).
33. Lieb, E. H. Residual entropy of square ice. *Phys. Rev.* **162**, 162 (1967).
34. Carrington, E. J. *et al.* Solvent-switchable continuous-breathing behaviour in a diamondoid metal–organic framework and its influence on CO_2 versus CH_4 selectivity. *Nat. Chem.* **9**, 882-889 (2017).

35. Sakata, Y. *et al.* Shape-memory nanopores induced in coordination frameworks by crystal downsizing. *Science*. **339**, 193-196 (2013).
36. Smallwood, I. *Handbook of organic solvent properties* (Butterworth-Heinemann, 2012).
37. Krause, S. *et al.* The effect of crystallite size on pressure amplification in switchable porous solids. *Nat. Commun.* **9**, 1573 (2018).
38. Kolbe, F. *et al.* High pressure in situ ^{129}Xe NMR spectroscopy: insights into switching mechanisms of flexible metal-organic frameworks isorecticular to DUT-49. *Chem. Mater.* **31**, 6193-6201 (2019).
39. Yuan, S. *et al.* Flexible zirconium metal - organic frameworks as bioinspired switchable catalysts. *Angew. Chem. Int. Ed.* **55**, 10776-10780 (2016).
40. Evans, J. D., Bon, V., Senkovska, I., Lee, H.-C. & Kaskel, S. Four-dimensional metal-organic frameworks. *Nat. Commun.* **11**, 2690 (2020).
41. Barnes, R., Torgeson, D.R. & Bray, P. J. On NMR powder spectrum simulation for nuclei with $I > 1/2$. *Phys. Status Solidi B*. **147**, K175-K178 (1988).
42. Schmidt-Rohr, K. & Spiess, H. W. *Multidimensional solid-state NMR and polymers* (Elsevier, 2012).
43. Spiess, H. W. Molecular dynamics of solid polymers as revealed by deutron NMR. *Colloid. Polym. Sci.* **261**, 193-209 (1983).
44. Spiess, H. W. & Sillescu, H. Solid echoes in the slow-motion region. *J. Magn. Reson.* **42**, 381-389 (1981).
45. O'Dell, L. A. & Schurko, R. W. QCPMG using adiabatic pulses for faster acquisition of ultra-wideline NMR spectra. *Chem. Phys. Lett.* **464**, 97-102 (2008).
46. Duer, M. J. *Introduction to solid-state NMR spectroscopy* (Wiley-Blackwell, 2005).
47. Simonov, A. & Goodwin, A. L. Designing disorder into crystalline materials. *Nat. Rev. Chem.* **4**, 657-673 (2020).

48. Macho, V., Brombacher, L., Graf, R. & Spiess, H. W. NMR WEBLAB. 2018
Available from: <https://weblab2.mpip-mainz.mpg.de/weblab66/>

Acknowledgements

The authors thank German Science Foundation (DFG) (FOR2433) for financial support. We thank HZB for the allocation of synchrotron radiation beamtime and financial support. VB thanks the BMBF (Project No. 05K19OD2) for financial support. TEG is grateful to DFG for financial support (project CRC 1279). JDE acknowledges the support of the Alexander von Humboldt foundation and HPC platforms provided by the Center for Information Services and High Performance Computing (ZIH) at TU Dresden. ALG gratefully acknowledges the European Research Council for financial support (Advanced Grant No. 788144). This project received funding from the European Union (EU) Horizon 2020 Research and Innovation Programme under Marie Skłodowska-Curie Grant Agreement 641887 (project acronym DEFNET).

Author contributions

SE and VB synthesized and characterized all materials by X-ray diffraction. MSW supported the collection of single crystal X-ray data. ER and ALG developed the disorder models. IS, TEG and UK analyzed the domain structure of nanocrystals based on TEM and electron diffraction data. JDE performed molecular simulations. MR and EB performed and interpreted the ^2H NMR spectra. MM and AP measured and interpreted the EPR spectra. ALG and SK initiated and scientifically guided the study. All authors contributed to writing and improving the manuscript.

Competing interests

The authors declare no competing interests.

Figure legends

Figure 1. Structure of DUT-8 and anomalous diffraction behaviour. a Columns of dabco-linked Ni_2 -paddle wheels are displaced vertically with respect to their neighbours as a consequence of the step-like nature of the 2,6-ndc ligand, the

distance of 1.2 Å indicates the step-height (grey: carbon, red: oxygen, green: nickel, white: hydrogen, blue: nitrogen). **b** Viewed down the column axis, the structure of DUT-8 is comprised of rhombic channels that, when fully open, are square in cross-section. **c** Representation of (hk1) reciprocal lattice planes, obtained from X-ray diffraction experiments on single-crystals solvated with NMP (top left), toluene (bottom left) and as made (DMF, right-hand), indicating the complex domain-type substructure. **d** The same combination of variability and complexity is evident in powder X-ray diffraction measurements, particularly in those regions marked by an asterisk (top-bottom solvated with *n*-heptane, NMP, acetone, toluene, ethanol, cyclohexane, DCM, DMF, CCl₄, chloroform).

Figure 2. Models of disorder in DUT-8. **a** Representations of the six possible channel arrangements containing two “up” and two “down” 2,6-ndc orientations as the channel is traversed in a clockwise sense (circular arrows). These arrangements partition into two sets based on the point symmetry at the channel centre (C_{2h} : circle and D_{2d} : square). Each arrangement can be associated with a corresponding jigsaw tile. **b** The corresponding configurational landscape of valid jigsaw tilings, mapped in terms of the parameters ϕ and η described in the text. Limiting (ordered) configurations occupy the vertices of the triangular phase diagram (corresponding unit cells shown in white outline, and space-group symmetries given below); a representative disordered state is shown in the centre of the diagram.

Figure 3. Experimental realisation of disordered DUT-8 states. **a** Comparison of experimental (grey lines) and best-fit calculated (coloured lines) powder X-ray diffraction patterns for DUT-8 samples loaded with a variety of different solvents (Supplementary Fig. 4-8). **b** Corresponding location of each sample in configurational space. The left inset shows the trajectory followed by a single sample during repeated guest exchange and the right inset shows the impact of varying solvent mixtures (DCM/*n*-heptane) on the disorder state. **c** Representative configurations and corresponding X-ray powder diffraction patterns associated with each step in this guest exchange process. **d** Representative configurations and corresponding X-ray powder diffraction patterns of different solvent mixtures.

Figure 4. Electron microscopy analysis of disordered DUT-8(Ni) nanocrystals. **a** An overview TEM image. **b** High resolution (HR) TEM image, and **c** corresponding power spectrum (Fourier transformation, FT) of the marked area. The HR image shows a crystal along [110]; the corresponding power spectrum contains reflections with the interplanar distances of 12.7 Å (characteristic PW–2,6-ndc–PW separation) and 9.5 Å (characteristic PW–dabco–PW separation), corresponding to (110) and (001) interplanar distances, respectively. Diffuse scattering along the $[1\bar{1}0]$ direction is evident. **d-f** The inverse Fourier transformation (IFT) analysis of the power spectra was performed using different positions of diffuse streak (1 - 3) shown in **c**. IFT area corresponds to the rectangular region marked in **b**. High-contrast patches in IFT patterns correspond to the crystal areas with the selected lattice fringes.

Figure 5. Characterization by NMR spectroscopy. **a** WURST Q-CPMG ²H NMR spectra of DUT-8(Ni) loaded with different solvents (*open pore*) and solvent free (desolv, *closed pore*). **b** Calculated 2D EXSY spectra for possible molecular

dynamics (calculations were performed for flips of a single isolated linker without implicit solvent interactions simulating the indicated flip angles using WEBLAB⁴⁸, see Methods section) c 2D EXSY NMR experiment for DUT-8(Ni) containing DMF (as made) measured for a mixing time t_m of 100 ms.

Tables

Table 1. Characteristic disorder configurations stimulated by solvent exchange.

Solvent	(ϕ, η)
Acetone	(0.2; 0.1)
Chloroform	(0.4; 0.0)
Cyclohexane	(0.3; 0.3)
Dichloromethane	(0.9; 0.7)
<i>N,N</i> -Dimethylformamide, (as made)	(0.4; 0.3)
<i>N,N</i> -Dimethylformamide, (exchanged)	(0.3; 0.1)
Ethanol	(0.4; 0.3)
<i>n</i> -Heptane	(0.3; 0.2)
<i>N</i> -Methyl-2-pyrrolidone	(0.1; 0.1)
Tetrachloromethane	(0.4; 0.0)
Toluene	(0.1; 0.1)

Methods

Synthesis of DUT-8(Ni)

The synthesis procedure was adapted from²⁸. Typically, $\text{Ni}(\text{NO}_3)_2 \cdot 6\text{H}_2\text{O}$ (404 mg, 1.4 mmol) is dissolved in 6 mL DMF, 2,6- H_2ndc (303 mg, 1.4 mmol) is dissolved in 15 mL DMF, and dabco (100 mg, 0.9 mmol) is dissolved in 9 mL MeOH. The resulting solutions are combined, transferred into a Teflon inlet, heated in an autoclave to 393 K and annealed for 48 hours. After cooling down, the supernatant reaction solution is removed by decantation and the dark green crystals are washed with fresh DMF several times.

For the deuterated DUT-8(Ni) the amount of starting materials was reduced. $\text{Ni}(\text{NO}_3)_2 \cdot 6\text{H}_2\text{O}$ (65.4 mg, 0.225 mmol) is dissolved in 1.4 mL *N,N*-dimethylformamide (DMF), d6-2,6- H_2ndc (50 mg, 0.225 mmol) is dissolved 3 mL DMF and dabco (16 mg, 0.14 mmol) is dissolved in 1.1 mL MeOH. The three resulting solutions are combined in a Teflon vessel (50 mL), heated in an autoclave to 393 K and annealed for 48 hours.

Synthesis of DUT-8(Ni) nanoparticles

Typically, $\text{Ni}(\text{NO}_3)_2 \cdot 6\text{H}_2\text{O}$ (434 mg, 1.50 mmol), 2,6- H_2ndc (294 mg, 1.36 mmol) and dabco (0.336 g, 3.00 mmol) were mixed and dissolved in 30 mL of DMF. After mixing of all the chemicals, a cloudy suspension was obtained, which was transferred to a Teflon-lined autoclave, placed into a preheated oven at 408 K and held at that temperature for 72 hours. The resulting particles were washed several times with fresh DMF.

Synthesis of mixed metal DUT-8($\text{Ni}_{0.98}\text{Co}_{0.02}$)

Typically, $\text{Co}(\text{NO}_3)_2 \cdot 6\text{H}_2\text{O}$ (75 mg, 0.028 mmol) were dissolved in 3 mL DMF, $\text{Ni}(\text{NO}_3)_2 \cdot 6\text{H}_2\text{O}$ (399.6 mg, 1.372 mmol) were dissolved in 3 mL DMF, 2,6- H_2ndc (303.4 mg, 1.4 mmol) is dissolved 15 mL DMF and dabco (100 mg, 0.9 mmol) were dissolved in 9 mL MeOH. The four resulting solutions were combined in a Teflon vessel (50 mL) and heated in an autoclave to 393 K and annealed for 48 hours. The resulting crystals were washed several times with fresh DMF.

Solvent Exchange

All polar solvents were exchanged directly from DMF. To obtain the samples loaded with non-polar solvents (*n*-heptane, cyclohexane and tetrachloromethane), DMF was firstly exchanged to DCM, due to the low miscibility of DMF and the respective solvents. DMF was removed by decantation and the crystals were suspended in the respective fresh solvent. The supernatant solution was removed several times in the first 2 hours and then every 12 hours for another 2 days. For the “repeated switching experiment” the solvent was exchanged 3 times within 30 minutes (Figure 3c,d).

Generation of the disorder models

The strikingly rich structural variety in DUT-8 arises from the step function implicit to the 2,6- ndc linker embedded in the DUT-8(Ni) framework structure (Figure 1a). DUT-8(Ni) belongs to the pillared layer structures, which in case of linear linkers typically form regular planar tetragonal (4,4) nets of composition $[\text{M}(\text{O}_2\text{C-R-CO}_2)_{4/2}]_\infty$ which are pillared by linear N-donor ligands (dabco). However, the step function in DUT-8(Ni) imposes deviations from planarity and considering the paddle wheel nodes the linker can form a step-up or step-down function. A straightforward representation of the step-function is an arrow pointing upwards (Extended Data Fig. 1).

In a periodic network structure, the registry requirement for closed loops places a non-trivial constraint on the vectors in that loop and it can be shown that only six local configurations are allowed. They can be classified into 4 equivalent configurations with local symmetry 2/m

(C_{2h}) which are related to each other by rotations around the 4-fold axis, in the following denoted as “Type 1” or “ C_{2h} ”, while 2 remaining configurations have $\bar{4}m2$ (D_{2d}) symmetry (“Type 2”).

Each loop may be also represented by a tile with characteristic tongue-groove orientation by rotating the arrows by 90° counter-clockwise (Extended Data Fig. 1). The equivalence of arrow-loops and coloured tiles is displayed in Extended Data Fig. 1. It is also important to note the implications of the periodic tiling on the local paddle wheel (PW) configuration (Extended Data Fig. 3). Each of the four ndc linkers connected to one PW may point upwards (+) or downwards (-) denoting the relative neighbouring orientation which allows for four different local PW configurations (**a**: + + + +, **b**: + + - -, **c**: + - + -, **d**: + - - -).

Each individual C_{2h} loop can tile space by itself to form a periodic arrangement with 2D crystal class m . Each PW cluster in this structure contains two 2,6-ndc pointing “up” and two pointing downwards in *cis*-orientation (or “+ + - -”, polymorph **B**, monoclinic, containing PWs **b**, local symmetry $2/m$, Extended Data Fig. 2)³². D_{2d} loops cannot by themselves tile space, instead the unique extended lattice containing D_{2d} configurations belongs to the 2D crystal class $4mm$. In this structure all 2,6-ndc linkers surrounding one PW have the same orientation (“+ + + +”, polymorph **A**, PW **a**), tetragonal, local symmetry $4mm$). The “up and down” orientation alternates between adjacent clusters.

A and **B** characterize the periodic structure of the polymorph obtained by arranging the tiles into a periodic pattern (Extended Data Fig. 2) while **a** and **b** denote the local arrangement of linkers for a single PW. Local arrangements **c** and **d** are formed in disordered configurations of tiles (Extended Data Fig. 3).

The six configurations (Extended Data Fig. 1) are equivalent to the six “2-in-2-out” states of

the square-ice spin model⁴⁹ with a finite configurational entropy $S_{config} = R \cdot \ln \left(\frac{4}{3} \right)^{\frac{3}{2}} \cong 0.43R$, hence favoring disorder in DUT-8 at 300 K by ca. 1 kJ/mole of Ni-dabco chains.

To rationalize an adequate disorder model, in a first approximation we only consider C_{2h} loops in a supercell. We assign the probability ϕ that denotes the likelihood of neighbouring rows/columns sharing opposite 2,6-ndc orientation. A probability $\phi = 0$ corresponds to the ordered m configuration (C_{2h} , m). A probability $\phi = 1$ gives another ordered configuration with tetragonal symmetry (2D crystal class $4mm$). Note, that this is another tetragonal variant without D_{2d} loops but containing PW **a** and **c** (“+ - + -”) with local symmetry $\bar{4}$ (Extended Data Fig. 3). A probability $\phi = 0.5$ gives a statistical distribution of row/column 2,6-ndc configurations. Interestingly, these intermediate ϕ values ($0 < \phi < 1$) generate the fourth PW variant **d** (Extended Data Fig. 3) with three 2,6-ndc linkers oriented in one direction (“+ - - -”). For a superstructure consisting of N PWs the number of possible combinations⁴⁹ is

W^N and $W = \left(\frac{4}{3} \right)^{\frac{3}{2}}$. This is the basis of disorder adaptivity providing a countably infinite number of disorder configurations as a response to a molecular stimulus. As orientations of the rows/columns may be indexed as a binary code, (01110) in principle the complex structural disorder in DUT-8 resembles a binary storage system.

As will be shown below, for the modelling of the experimentally observed powder patterns it is necessary to construct models containing interspersed D_{2d} loops. They are essentially generated by flipping individual arrows in a C_{2h} -loop-only configuration. The relative fraction of D_{2d} loops is η .

A representative real world structure as a paradigmatic 16x16 supercell, originally composed of C_{2h} -loops (original row/columns orientations indicated with grey arrow) is shown in Extended Data Fig. 4. Flipping individual arrows in this example (indicated by red arrows) creates tetragonal microdomains composed of D_{2d} -loops and domain walls at the intersection. The center of the tetragonal microdomains is located at the intersection of the

type 1 domain boundaries. Representations of the configurational space and the resulting undulation are displayed in Extended Data Fig. 5.

Single crystal X-ray analysis of “as made” single crystals

The main feature of DUT-8(Ni) structure is a non-linearity of the 2,6-ndc²⁻ linker. This leads to a systematic stepwise relocation of pillars in the crystal structure with a constant value of 1.2 Å, dictated by quasi-linear 2,6-naphthalene core. The crystal structure of DUT-8(Ni) was initially determined in 2010 by single crystal X-ray diffraction²⁵. The tetragonal space group *P4/n* was chosen for the structure solution and refinement, although symmetry of the structure is compatible with high symmetrical space group *P4/nmm*. Authors fairly admitted high R-values ($R_{int} = 0.2694$, $R_1 (I > 2\sigma(I)) = 0.1546$, $wR_2 (all\ data) = 0.3428$ after SQUEEZE). The local coordination environment of the paddle wheel (PW) is built by four equally oriented 2,6-ndc²⁻ linkers, directed by the 4-fold rotation axis. The crystal structure of the closed pore (cp) phase was solved from single crystal X-ray diffraction in triclinic symmetry and further refined based on powder X-ray diffraction data. Interestingly, in this case only the conformation with alternating ligand steps could be achieved²⁴. Heine and co-workers considered both conformations, called polymorph A (equal to initially published in 2010) and polymorph B (reported in 2015) and suggested the most appropriate closing mechanism involving the structures of conformer B³². The results were also supported by an experimental structure, derived from single crystal data. The structure of polymorph B was refined in the monoclinic space group *C2/m* with acceptable final reliability parameters ($R_{int} = 0.0581$, $R_1 (I > 2\sigma(I)) = 0.0826$, $wR_2 (all\ data) = 0.2625$), but considering pseudo-merohedral twinning in the sample (rotation matrix 1 0 0.5 0 -1 0 0 0 -1). All these findings confirm the complexity of the crystal structure of DUT-8(Ni) and stimulated us to deeper investigate the domain structure in the system. As a first step we reinvestigated the data reported in 2010²⁵. Careful analysis of (hk0), (hk1), (hk2) and (hk3) lattice planes indicate the co-existence of multiple domains in the single crystal (Extended Data Fig. 6).

Depending on the lattice selection, the dataset was processed in tetragonal (*P4/nmm*) and monoclinic (*C2/m*) symmetry. In both cases, the crystal structure was solved by direct methods and refined by least-squares on F^2 using SHELX-2018⁵⁰. The corresponding structural models correspond to conformers A and B, discussed elsewhere in detail³². Similar unit cell volumes for both structural models allow their co-existence within the same single crystal. The convergence parameters of the refinement in both cases are not acceptable in terms of reliability factors and residual electron density, which cannot be attributed to chemically reasonable atom positions of the structures (Supplementary table 2). Since both monoclinic and tetragonal domains are simultaneously present in the reciprocal space leading to overlapping in numerous reciprocal lattice planes, we decided not to continue further analysis of the data (Supplementary Section 3). CCDC-1989709 and CCDC-1989708 contain the supplementary crystallographic data for DUT-8(Ni) polymorph A and DUT-8(Ni) polymorph B, respectively. ORTEP diagrams show the asymmetric units of both structures are shown in Supplementary Fig. 1.

Single crystal X-ray analysis of solvent exchanged single crystals

Single crystals of DUT-8(Ni) were analysed, in which DMF guest molecules were exchanged by N-methyl-2-pyrrolidone (NMP) or toluene. According to PXRD patterns, these samples contain predominantly C_{2h} loops ($\phi = 0.1$, $\eta = 0.1$), which can be treated in the refinement as pseudo-merohedral twins with partially overlapped reciprocal lattices. The datasets were collected at BL14.3 beamline of the BESSY-II synchrotron.⁵¹ For each single crystal, 180 images were collected in a φ -scan mode with an oscillation angle of $\Delta\varphi = 1^\circ$. A Rayonix MX-225 detector at 55 mm distance was used to collect the 2D images with 1.2 s exposition. The collected images were processed in automatic mode using XDSAPP 2.0 software.⁵²

Alternatively, images were converted in .sfrm format and four partially overlapped monoclinic C-centred lattices were found using CELL_NOW program⁵³. The images of (hk0), (hk1), (hk2) reciprocal planes confirm the presence of four different domains in both single crystals (Extended Data Fig. 7). The intensities were extracted using SAINT software⁵⁴ and corrected for absorption, Lorentz and polarization effects using TWINABS program⁵⁵. Two separate files, one containing structural factors from single domain for structure solution (HKLF4 format) and second with reflections of all four domains for structure refinement (HKLF5 format) were generated. The structures were solved using direct methods and refined by least-squares on F^2 using SHELX-2018/3 software⁵⁰. The dabco molecules show dynamic disorder with 8 separate positions for three carbon atoms and therefore refined with occupancies 3/8 for each general position. The volume fractions of each domain in the structure were refined as free variables resulting in a ratio 0.325(4) / 0.325(4) / 0.209(3) / 0.141(3) for NMP@DUT-8(Ni) crystal and 0.297(4) / 0.294(4) / 0.200(3) / 0.209 (3) for toluene@DUT-8(Ni). CCDC- 1989557-1989560 contain the supplementary crystallographic data for NMP@DUT-8(Ni) and toluene@DUT-8(Ni), respectively (Supplementary Table 3). The ORTEP diagrams of asymmetric unit for all structures are shown in Supplementary Fig. 1.

Calculation and matching of X-ray powder diffraction patterns

A custom Monte Carlo code was implemented to generate DUT-8 configurations of arbitrary size with specific (ϕ, η) characteristics. Simulations were initialized in the type 2 (D_{2d}) phase. Monte Carlo steps involved the 'long loop' algorithm, which ensured that square ice rules were strictly obeyed at all times⁵⁶. The Monte Carlo criterion was based on the difference between calculated and target (ϕ, η) values. The simulation was terminated when the target (ϕ, η) value of interest was reached. Simulation boxes of 40 x 40 supercells were used. At this size, the increasingly ordered configurations were difficult to access, which is why we had difficulty obtaining configurations corresponding to the edges of the phase triangle (Figure 3b). For each generated DUT-8 configuration a model was simulated using a Monte Carlo approach. This model contains a single atom at the vertex of each pore: this corresponds to the midpoint of the Ni-carboxylate paddle wheel. There is also an atom at the center of each 2,6-ndc unit. We used atom types Nd and Y, respectively, for these two positions since the ratio of atomic masses reflects approximately the ratio of the scattering density of the paddle wheel and 2,6-ndc units. The unit cell parameters were calculated by taking into account the number of up/down vertical shifts along each direction of the supercell. No attempt was made to convert cells and coordinates into conventional space group form. For each configuration corresponding X-ray diffraction patterns were calculated ($\lambda = 1.5406 \text{ \AA}$) using the program CrystalDiffact (Figure 3a, Supplementary Fig. 2-8). A peak width of 0.15° was used. We show here the form of the diffraction pattern for $9^\circ \leq 2\theta \leq 18^\circ$ for our various Monte Carlo configurations (Supplementary Fig. 2).

The use of coarse-grained models was validated by comparison with explicit models. As very large atomistic models are needed to account for the observed correlated-disordered structures ($> 2,000,000 \text{ \AA}^3$) and the associated computational effort is expensive this validation was performed only for a representative set of ϕ, η parameters (Supplementary Fig. 3). As there is no meaningful difference in diffuse scattering profiles between the two, the use of coarse-grained profiles to identify ϕ, η parameters for DUT-8(Ni) samples is reasonable. In terms of interpreting total scattering data, coarse graining is equivalent to deconvolution by the molecular form factor, which affects scattering intensities but not the basic form of the diffuse scattering⁵⁷.

The experimental data sets provided were prepared for comparison by removal of a linear background and rescaling to uniform total integrated intensity across the $9^\circ \leq 2\theta \leq 18^\circ$ region (Supplementary Fig. 4-8). We explored using a number of quantitative approaches by which to automatically match experiment with calculated patterns, but because of subtle variation in peak positions and the inability to match quantitatively the (Bragg) peak intensities, it was not possible to arrive at a universally acceptable solution. Instead we matched patterns by visual comparison.

It is perhaps worth emphasising that the entire ensemble of fits shown in Figure 3 involves a total of 24 parameters: the peak width, the three structural parameters shown above for the basic connectivity, and the pair of (ϕ, η) parameters for each phase. The values of these disorder parameters are given in table 1.

For some cases these assignments can be made uniquely with confidence; for others there is more than one pair of ϕ, η -values that could account for the observed diffraction pattern. This is probably most severe for the cases of CHCl_3 , CCl_4 , and DMF.

Samples containing low boiling solvents (CH_2Cl_2 , CHCl_3 , CCl_4) in Figure 3a were prepared in capillaries (measurement time 16-24h). For the dynamic exchange demonstrated in Figure 3c, in order to measure a pattern directly after the exchange, the samples were prepared between aluminium coated polyester foils and measured within 30 minutes.

In Extended Data Fig. 5 these distinct disorder patterns characteristic for each solvent are located in the ϕ, η triangle and pictorial representations for each disorder pattern are displayed for representative solvents.

Electron diffraction and high resolution electron microscopy

Samples for TEM investigations were prepared by dropping the DUT-8(Ni) nanoparticles suspended in DMF onto a carbon coated copper grid and dried at room temperature. TEM studies were performed using a Thermofisher TITAN TEM operated at 300 kV with a Cs-corrector on objective side. High-resolution TEM images were collected at a nominal magnification of 69kx, at electron dose of $11 \text{ e}/\text{\AA}^2$ per image. The magnification and dose rate were adjusted in order to match the characteristic dose⁵⁸ of the material, being measured as $10 \text{ e}/\text{\AA}^2$. The images were collected using a self-written Digital Micrograph (GATAN, Pleasanton, USA) script, shifting the TEM stage in a regular grid, thus assuring data collection from a fresh, previously unexposed area. A delay was built into the script after the stage shift before the exposure, in order to minimize the stage-movement induced sample drift. Electron diffraction patterns were collected in nanodiffraction mode with a S2 aperture of $50 \mu\text{m}$ and an effective beam diameter on the sample of 250 nm . Electron diffraction data were collected using the Digital Micrograph script shifting the stage (see above). Kinematically simulated electron diffraction patterns of a known structure were produced using eMap (AnaliTEX, Stockholm, Sweden) software.

A typical electron diffraction pattern of an as made (DMF) DUT-8(Ni) nanocrystal is shown in Extended Data Fig. 8. The pattern contains the $(1\bar{1}0)$ axis oriented vertically. Extended Data Fig. 8 shows a simulated pattern of the $[110]$ crystallographic zone of the tetragonal structure. The $(1\bar{1}0)$ axis is oriented vertically, the c^* axis is horizontal. This zone, however does not match the experimentally observed pattern – there are no experimental reflections on the horizontal c^* axis, instead discrete reflections appear above and below the horizontal dashed line (marked with arrows in Extended Data Fig. 8). This situation is achieved when the crystal is rotated around the $(1\bar{1}0)$ axis, for instance to the $[331]$ crystallographic zone shown in Extended Data Fig. 8. Additionally, the intensity distribution in the top part of the experimental pattern does not match that of the bottom part, implying additional slight tilt around the horizontal axis. Thus, the experimentally observed pattern is a slight off-tilt of the $[110]$ zone in an arbitrary direction.

In the experimental pattern the diffuse scattering along the $(1\bar{1}0)$ is evident. The diffuse scattering does not affect the central $(1\bar{1}0)$ reflections row. The first row contains slightly elongated reflections, while the second row appears as a short diffuse line.

^2H solid state NMR spectra simulation

Calculations of the expected deuterium 2D EXSY spectra were carried out using the software NMR Weblab⁴⁸ for a coupling constant of 128 kHz, an electric field gradient tensor of zero asymmetry, and a cone angle of 60°. The cone angle is the angle between the linker rotation axis and the C- ^2H bond vector. Calculations were made for linker jump angles ϕ of 0° (no jumps, i.e., immobile linker), 90°, 120° and 180° as indicated. Note that the presence or absence of solvent molecules is not of importance for this simulation. The agreement between the experimental spectrum and the spectrum without jumps (0°) proves the linker immobilization at the time scale of the mixing time. Otherwise, non-diagonal intensity would be observed similar to the spectra with non-zero jumps.

References (methods)

49. Nagle, J. Theory of the dielectric constant of ice. *Chem. Phys.* **43**, 317-328 (1979).
50. Sheldrick, G. M. Crystal structure refinement with SHELXL. *Acta Cryst. C.* **71**, 3-8 (2015).
51. Gerlach, M. *et al.* The MX beamlines BL14. 1-3 at BESSY II. *J. large-scale Res. Facil.* **2**, 47 (2016).
52. Sparta, K. M. *et al.* XDSAPP2. 0. *J. Appl. Cryst.* **49**, 1085-1092 (2016).
53. Sheldrick, G. CELL_NOW, version 2008/4. *Georg-August-Universitat Göttingen: Göttingen, Germany.* (2008).
54. SAINT, V. 8.34 A. *Bruker AXS Inc.: Madison, WI.* (2014).
55. Sheldrick, G. M. *TWINABS. Ver. 2012/1.* (2012).
56. Barkema, G. & Newman, M. Monte Carlo simulation of ice models. *Phys. Rev. E.* **57**, 1155 (1998).
57. Schmidt, E. & Neder, R. B. Diffuse single-crystal scattering corrected for molecular form factor effects. *Acta Cryst. A.* **73**, 231-237 (2017).

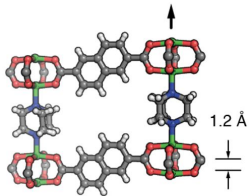
58. Kohl, H. & Reimer, L. *Transmission electron microscopy: physics of image formation* (Springer, 2008).

Data availability

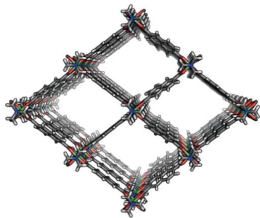
The data supporting the findings of this study are available within the article and the supplementary materials. The corresponding raw data are available from the corresponding authors. Single crystal structures can be obtained free of charge from the Cambridge Crystallographic Data Centre via www.ccdc.cam.ac.uk/data_request/cif. CCDC-1989709 and CCDC-1989708 contain the supplementary crystallographic data for DMF@DUT-8(Ni) of polymorph A and DMF@DUT-8(Ni) polymorph B, respectively. CCDC- 1989557-1989560 contain the supplementary crystallographic data for NMP@DUT-8(Ni) and toluene@DUT-8(Ni), respectively. For each solvent two independent refinements are provided considering a single domain crystal or a four-component twin as explained in the methods section and supplementary information.

Code availability

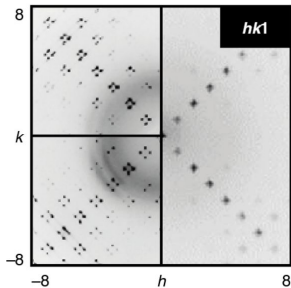
All custom code used for the disorder analysis in this study was developed using widely-available algorithms. Copies of the actual code used can be obtained upon request from ALG. Computational data supporting the findings in Supplementary Section 10 are available from the public GitHub online repository at <https://github.com/jackevansadl/supp-data>.



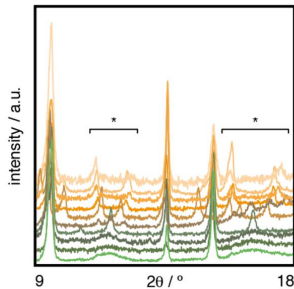
a



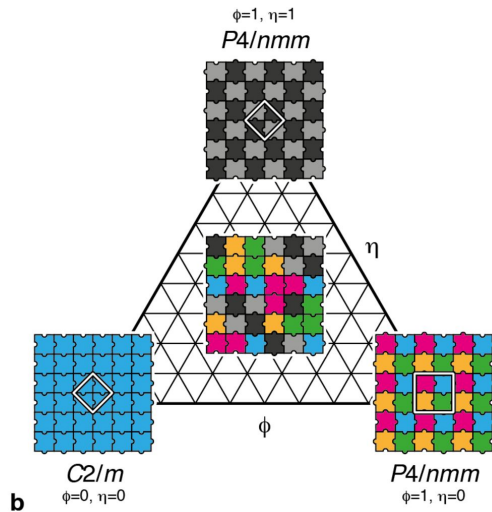
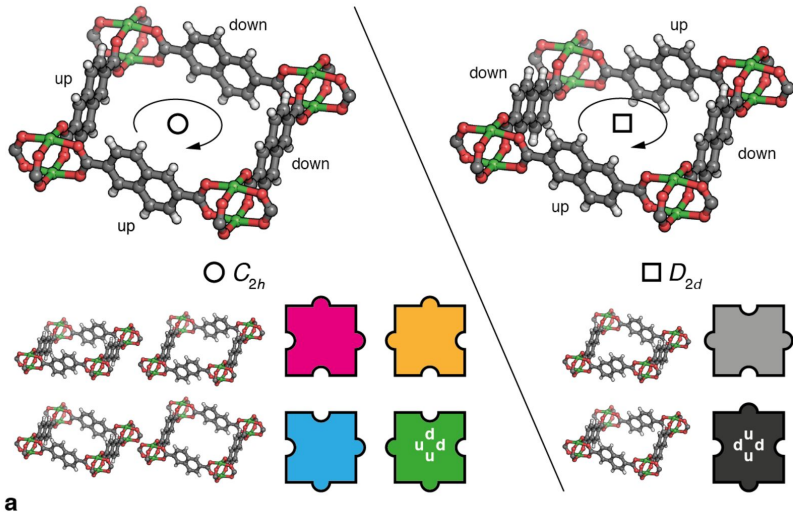
b

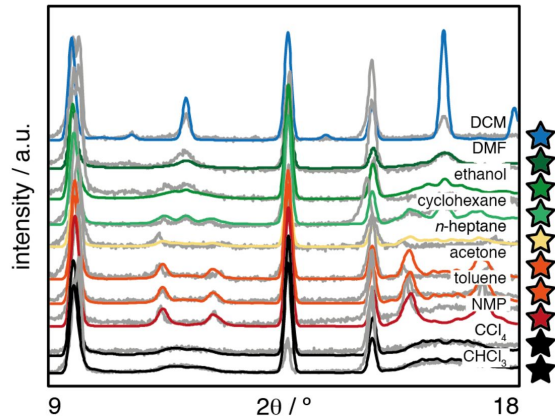


c

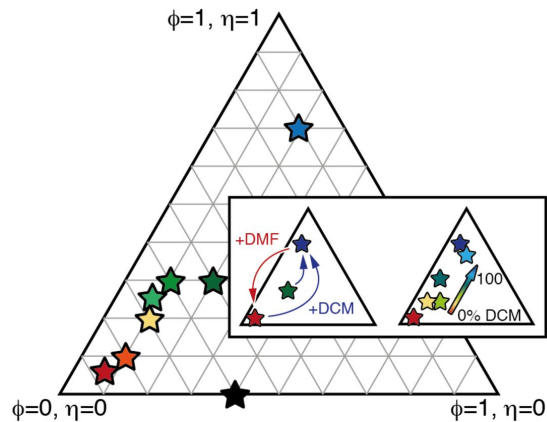


d

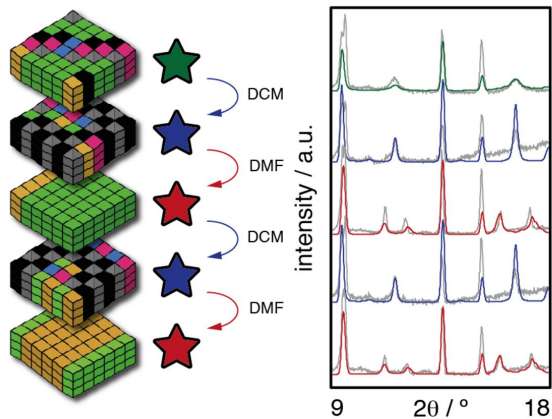




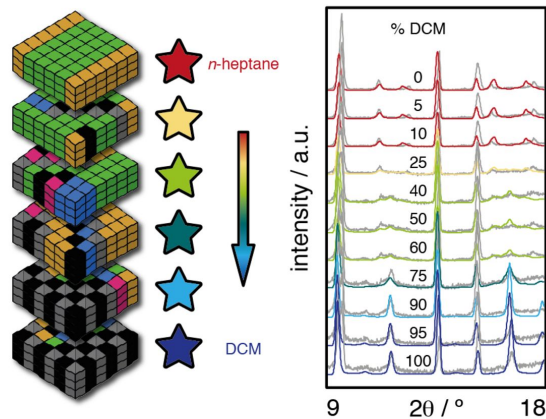
a



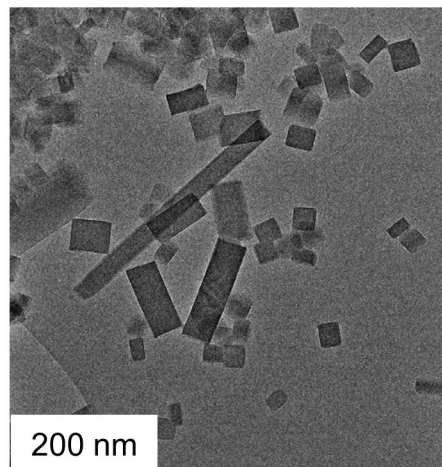
b



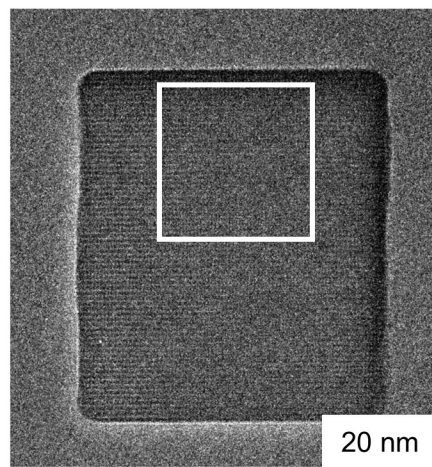
c



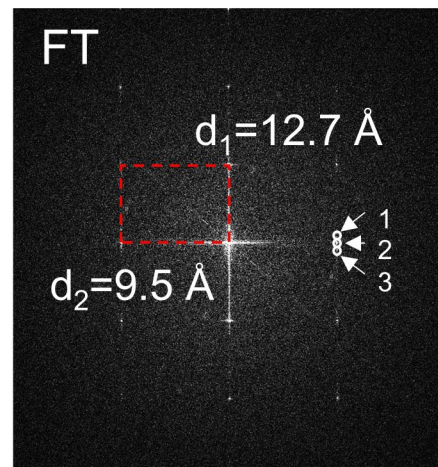
d



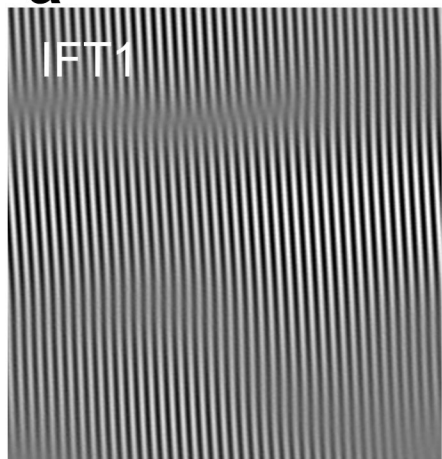
a



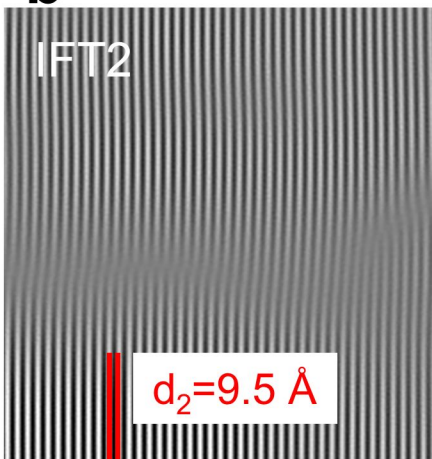
b



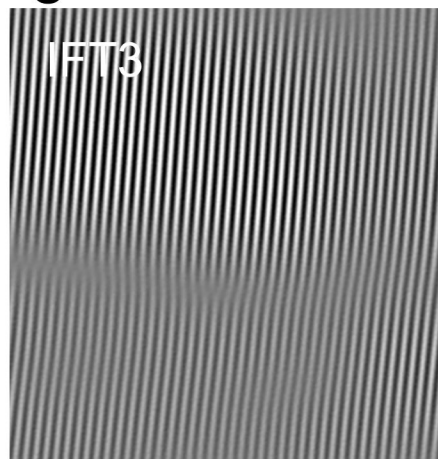
c



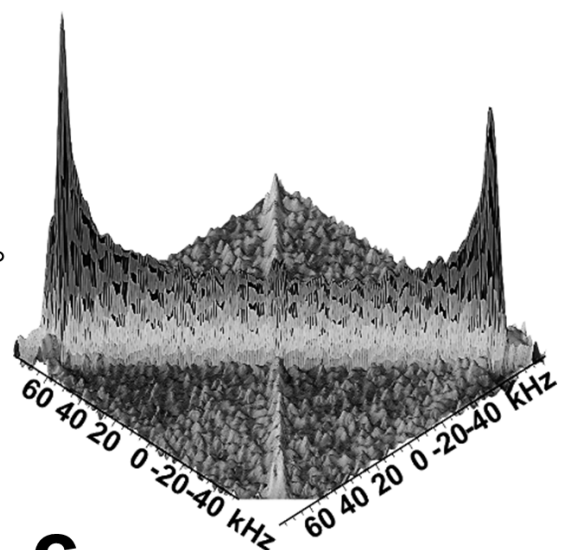
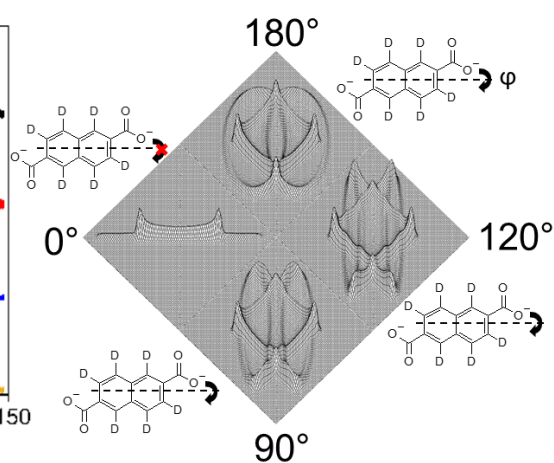
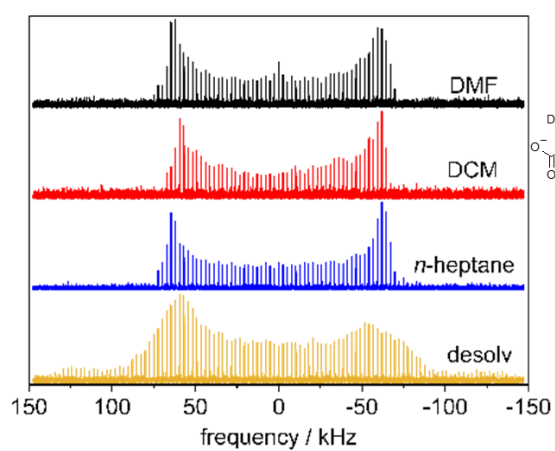
d



e



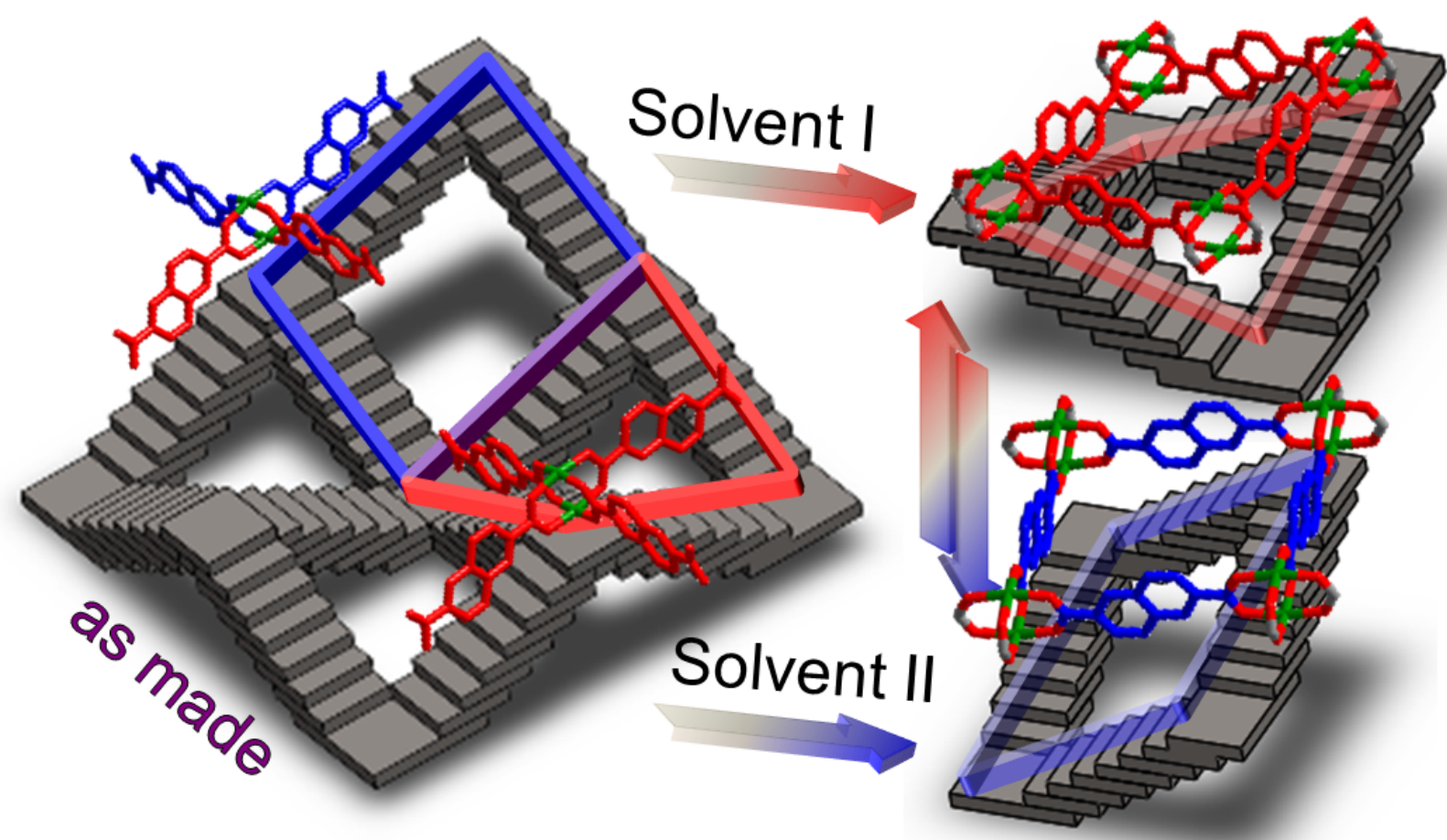
f



a

b

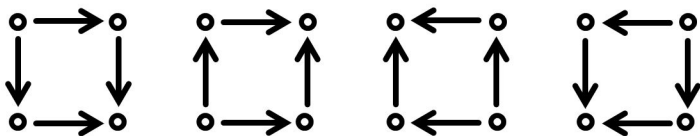
c



Type 1 (C_{2h})

Type 2 (D_{2d})

a



1

2

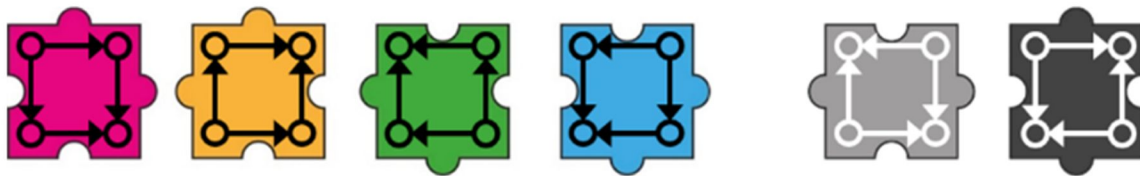
3

4

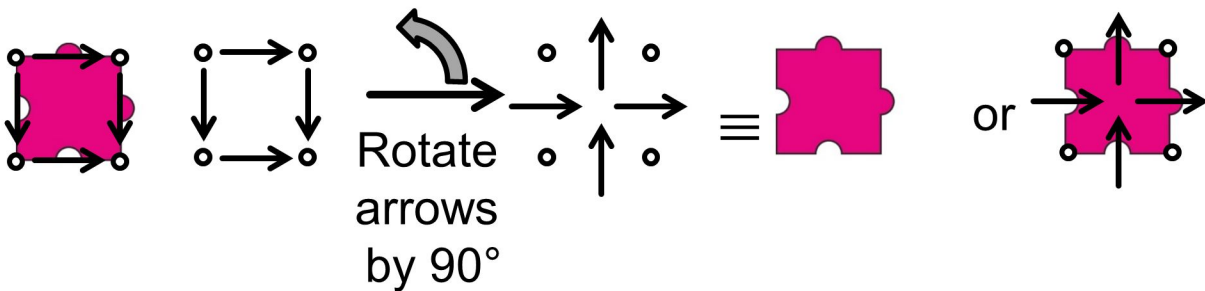
5

6

b

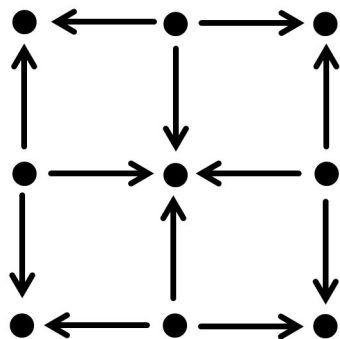


c

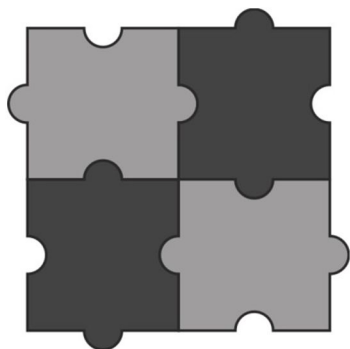


Polymorph A

$D_{2d}: 4mm$

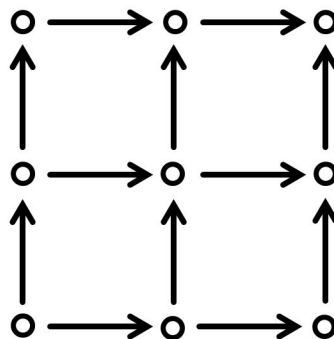


● = a

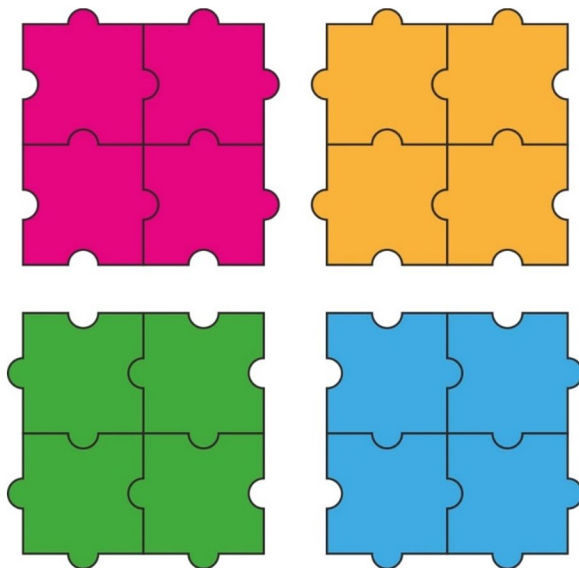


Polymorph B

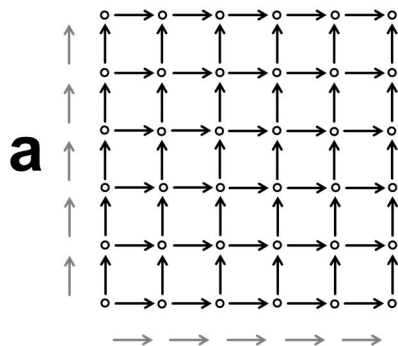
$C_{2h}: m$



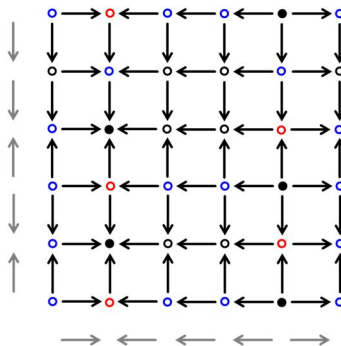
○ = b



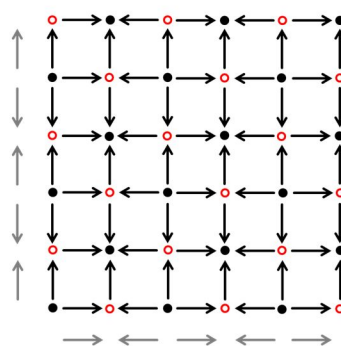
Type 1, $\phi = 0$



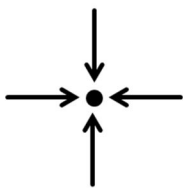
Type 1, $0 < \phi < 1$



Type 1, $\phi = 1$

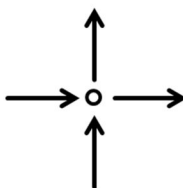


b



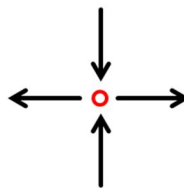
● = a

+ + + +



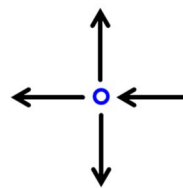
○ = b

+ + - -



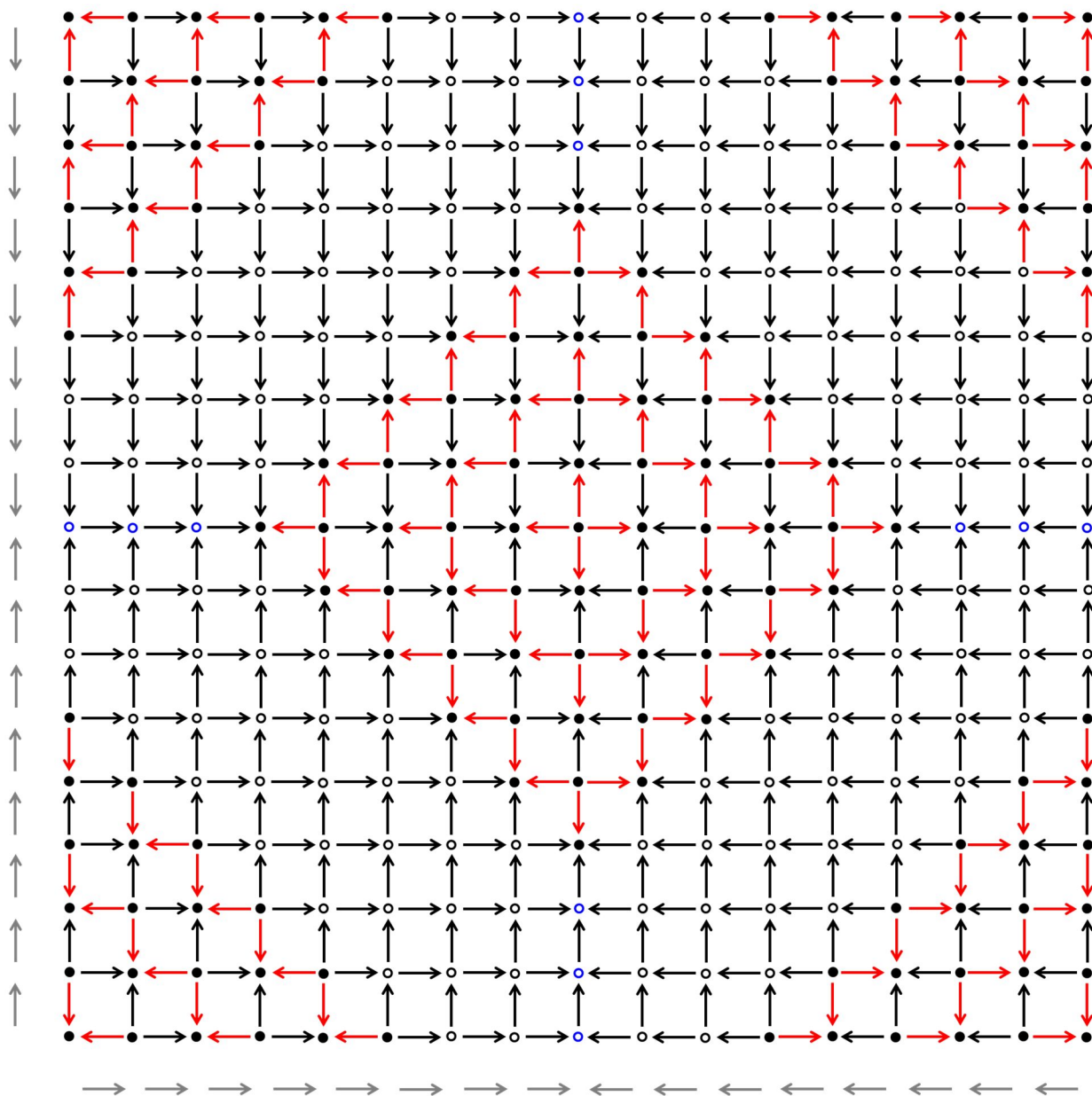
○ = c

+ - + -

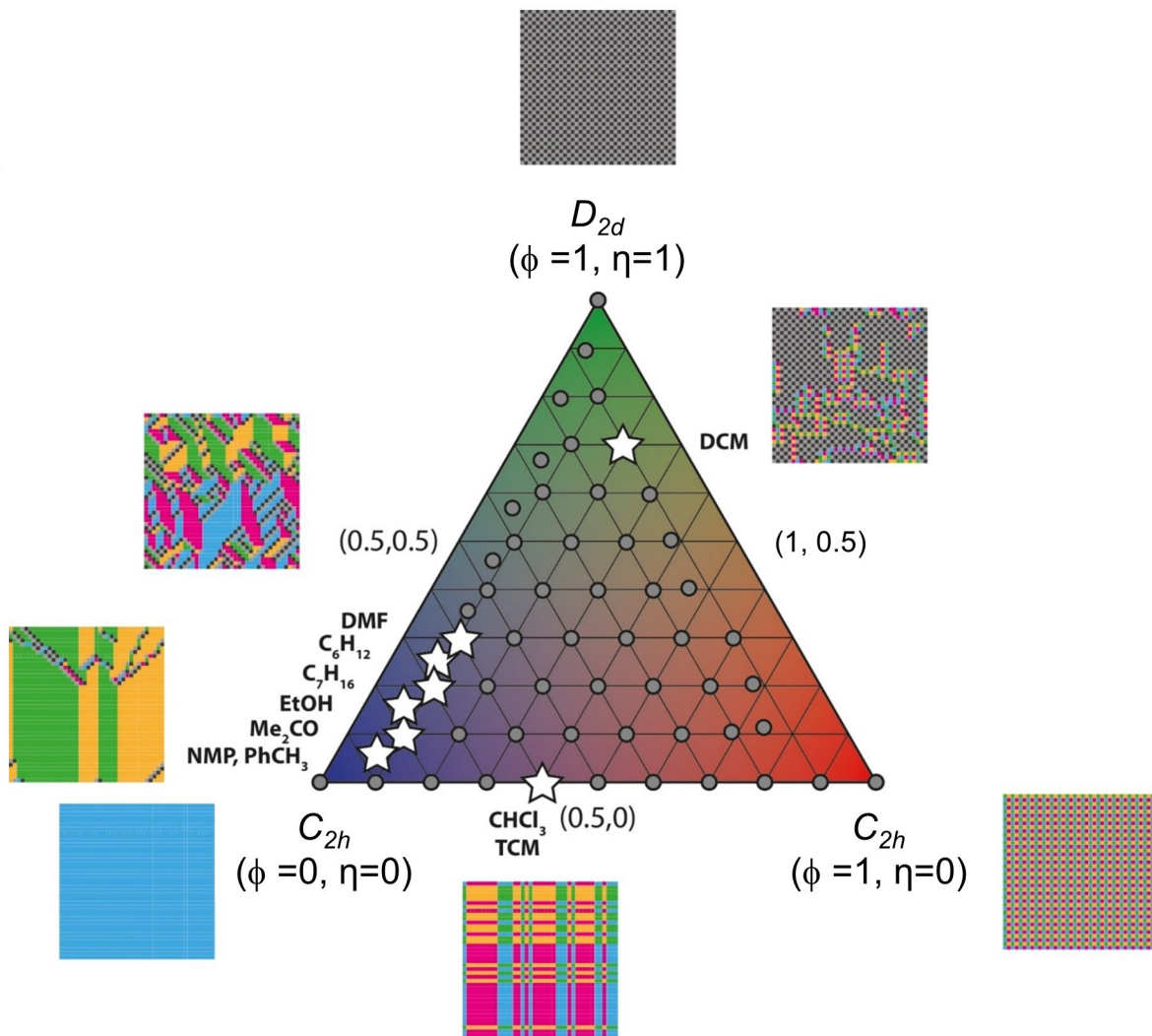


○ = d

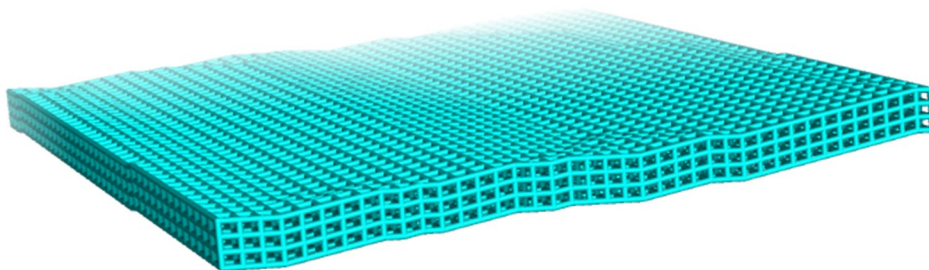
+ - - -

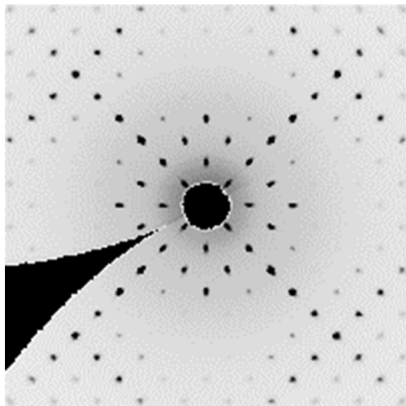


a

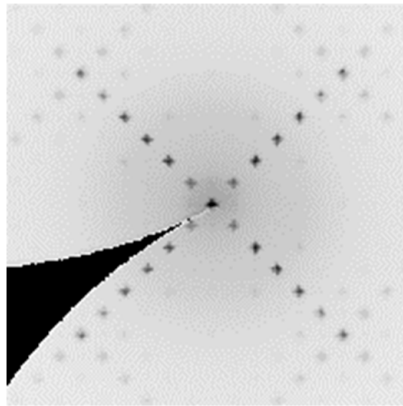


b

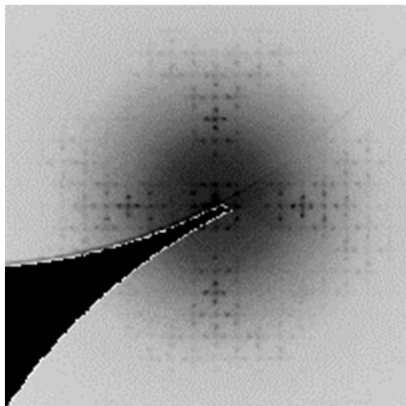




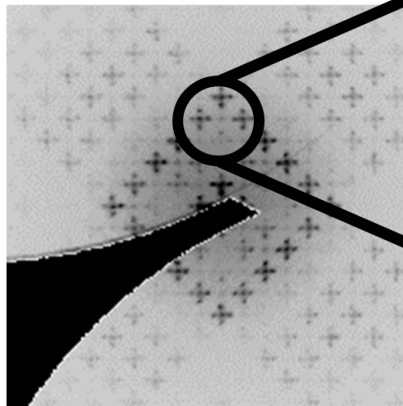
(hk0)



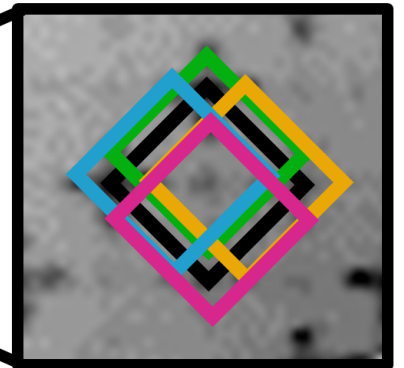
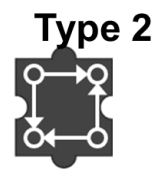
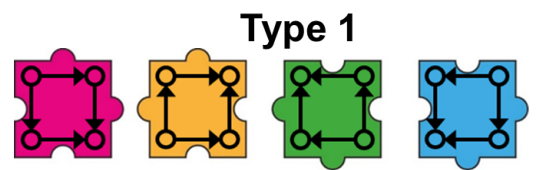
(hk1)



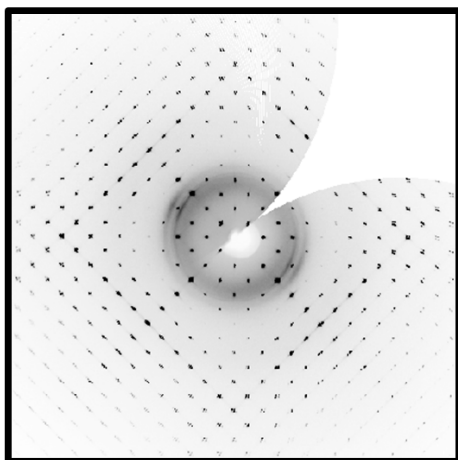
(hk2)



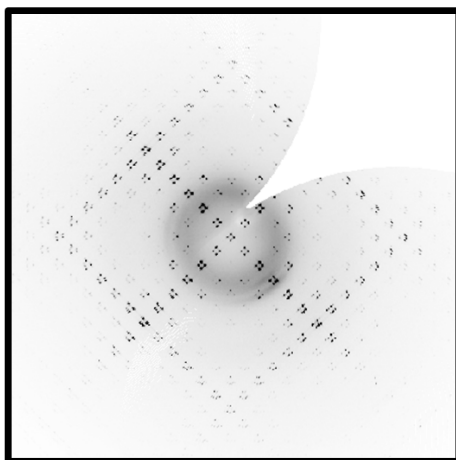
(hk3)



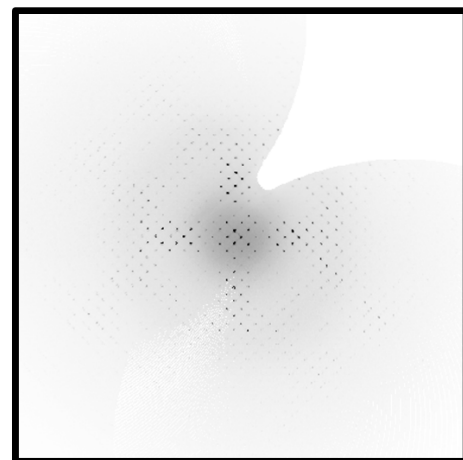
a



(hk0)

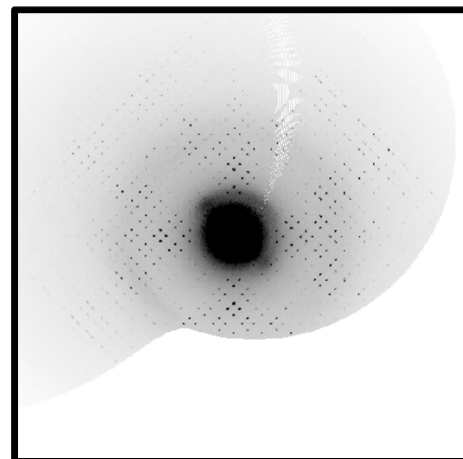
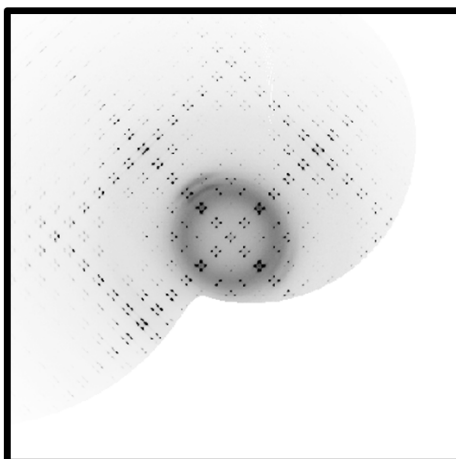
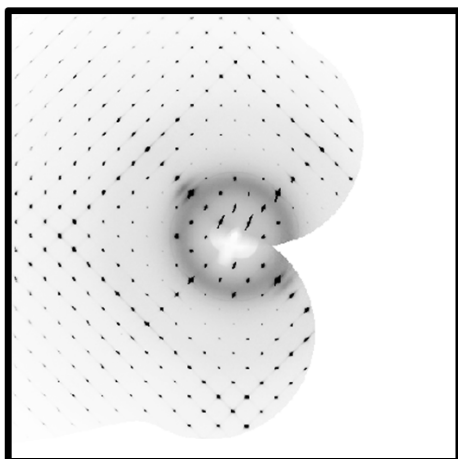


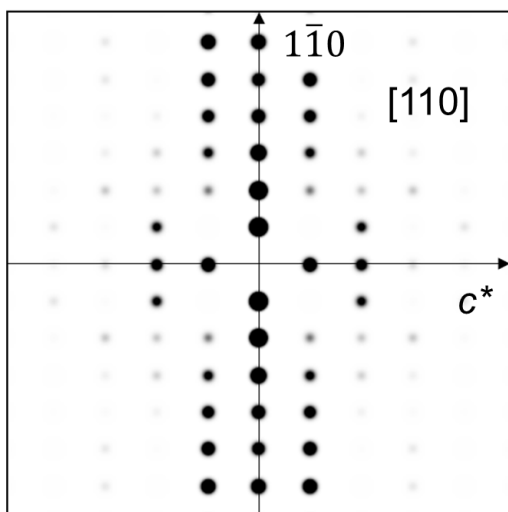
(hk1)



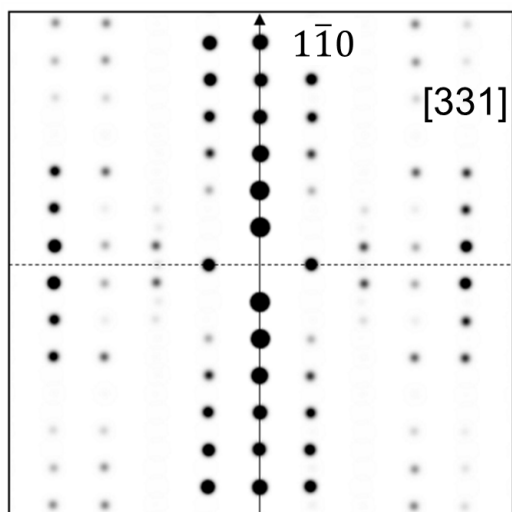
(hk2)

b

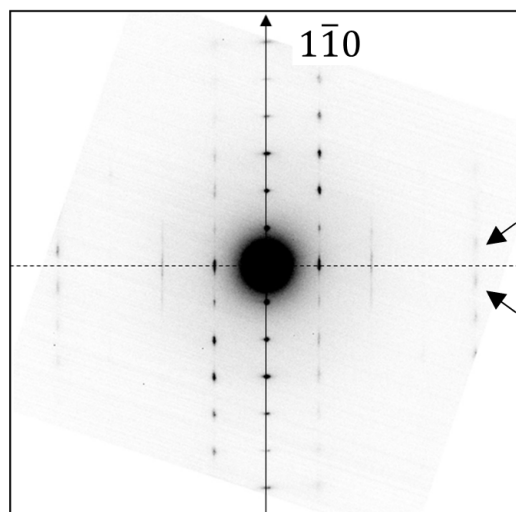




a



b



c

